1.5	0.4889	0.9836
2	1.5759	0.9474

In this study, the paper of Ahn(2021) was cited for the analysis of the rheological behavior of SA solution(Ahn et al., 2021). Fig.1 indicates the rheological behavior of SA solution. In the case of Fig.1(a), as the concentration of SA increased, the apparent viscosity showed a tendency to increase. In particular, when the concentration of SA was 2% or more, the apparent viscosity increased rapidly as the concentration increased. This caused an increase in gelation between particles as the concentration increased. Fig.1(b) indicates that all SA solutions showed a shear thinning tendency among non-Newtonian fluids where the shear stress increased as the shear rate increased.

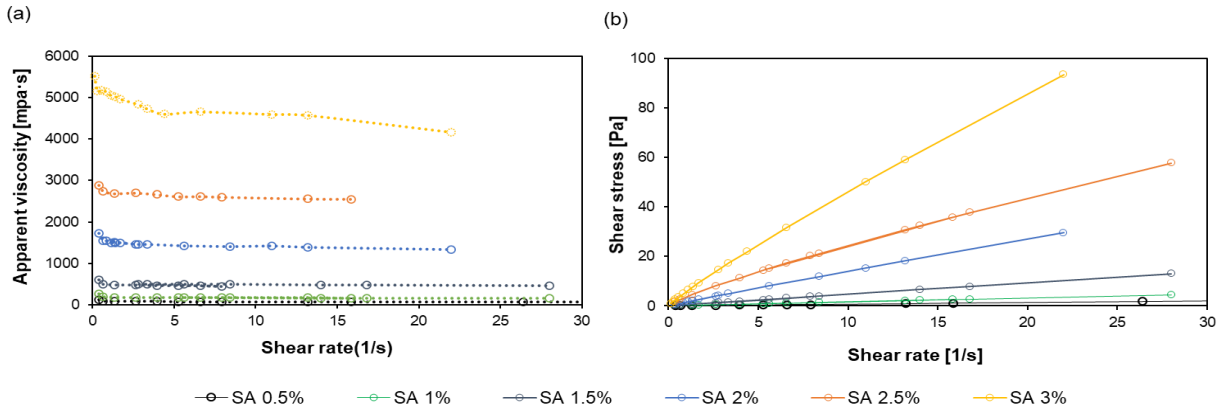

Fig.1 Rheological behavior of SA solution (a): apparent viscosity (b) shear stress (power-law fitting)

2.2 Non-newtonian fluid flow

In microscopic view, the pore consists of a body and a throat. In pipe flow, Poiseuille flow and shear-thinning flow will flow as shown in Fig. 2(Lenci et al., 2020). If pipe flow is assumed for pore throat flow analysis, it is judged that fluid flow in porous media will also show a similar flow behavior.

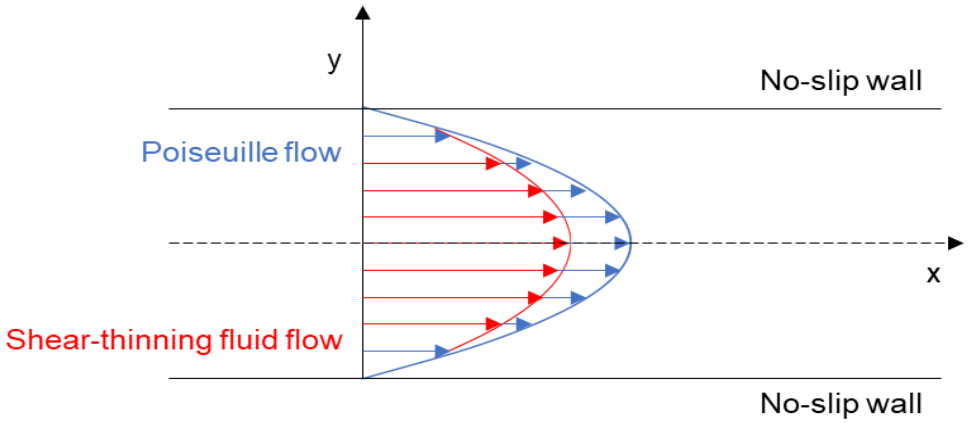

Fig.2 Fluid flow behavior between Poiseuille and Shear-thinning flow

3. Materials and methods

3.1 Materials

SA (sodium alginate, MP Biomedicals, USA) used in this paper is produced by alginic acid originating from brown seaweed. Alginic acid is composed of mannuronic acid and L-guluronic acid, and the molecular structure is shown in Fig.3. For the SA solution to be used in the experiment, a magnetic stirrer was used by mixing distilled water and SA powder, and an equal SA solution was prepared by introducing a stirring time of 24 hours at 60RPM.

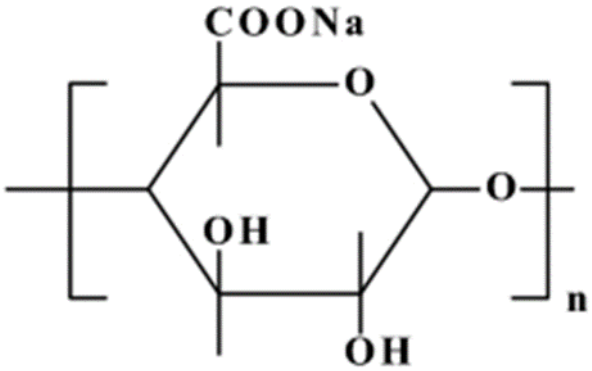

Fig.3 Molecule structure of Sodium alginate(Sahoo and Biswal, 2021)

3.2 Micro-scale test

A micro-scale test was performed to analyze the injection characteristics of the SA solution. For the injection of the fluid, a syringe pump (Syringe pump, Kats Scientific, NE-1010) capable of controlling the volumetric flow rate of the fluid was used. The micromodel used in this study was created by overlapping the two symmetrical silicon dioxide (SiO2) glass plate, which can similarly be implemented on the surface characteristics of the clay particles. A micro-scale test is an experiment to analyze the pore saturation of the remaining fluid after the DI or SA solution pushes out the air saturated with the microfluidic device. Experiments were performed with single-phase fluid flow in an air-saturated state. In the test, 100PV was injected until the pore change in the microfluidic device due to the injected solution (DI or S.A solution) did not occur. Before all experiments were performed, the microfluidic device was cleaned by flooding DI to minimize the experimental error caused by foreign substances remaining in the microfluidic device. In this study, it was difficult to inject more than 2.5% of SA solution linearly due to high viscosity. Therefore, 0.5%, 1%, 1.5%, and 2% of SA solution were used for the test. In addition, the volumetric flow rate was changed to 1, 10, 100, and 1000 μL/min through a syringe pump to analyze the saturation and correlation. Results for image analysis to obtain the videos and photo with high resolution cameras. The schematic diagram of the overall micro-scale test is as follows.

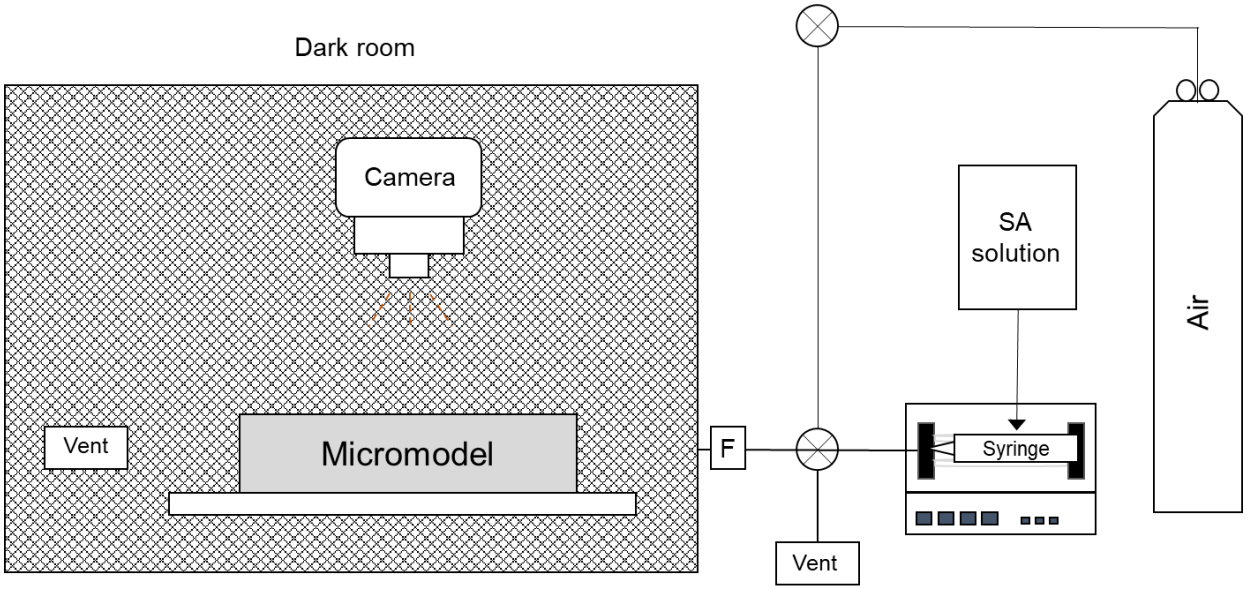

Fig.4 Schematic diagram of micro-scale test

3.3 Image processing

In the raw image obtained through the experiment, it is necessary to reduce the errors due to light and the vertical and horizontal difference of the image. The raw image treatment process for image analysis was performed through conversion, filtering, and thresholding of the acquired raw[Fig.5]. Fig. 5(a) shows the raw image of the micro model

before injection. Fig. 5(b) shows the image processing using the image filter on the raw image. Through image filtering, solid(white) and pore(black) were clearly distinguished. Fig. 5(c). was used to calculate the fraction through thresholding on the filtered image. Fig. 5(d), (e), (f) shows image processing photos after injection, respectively. Finally, the error between the thresholding-processed image and the raw image was improved through visual analysis between mutual images. After the fluid injection was completed through the final image obtained, the saturation was calculated through the pixel fraction of the injected fluid and the air remaining inside the micromodel.

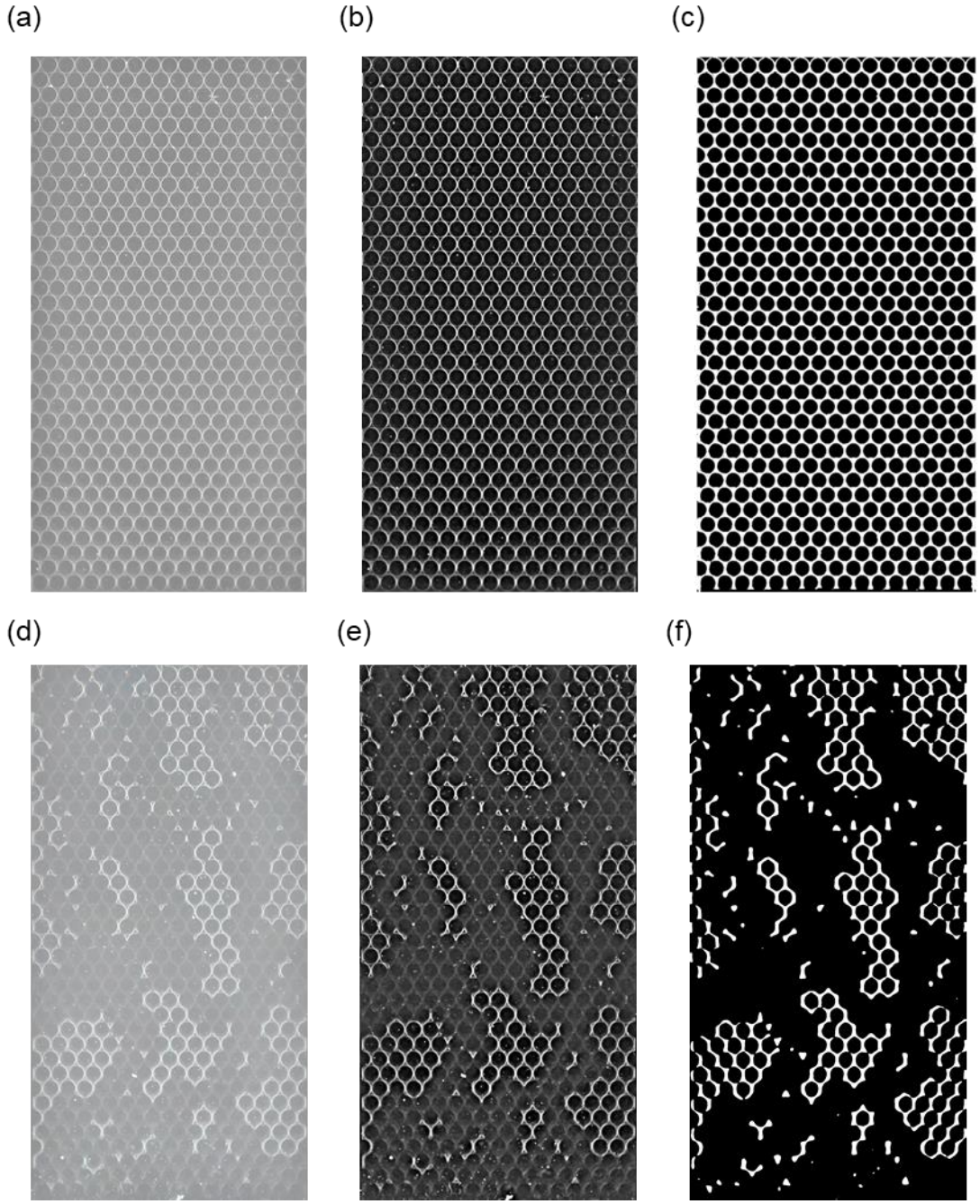

Fig.5 Image processing (a): Raw image before injection (b) filtering image before injection (c) image treatment (d) : Raw image after injection (e) filtering image after injection (f) image treatment

4. Results

4.1 Pore saturation

Fig 6. shows the pore saturation change with the volumetric flow rate and SA concentration. For all fluids, the pore saturation tends to increase as the volumetric flow rate increases. In the case of water, when the injection flow rate was 1 to 1000 μL/min, the saturation was 66.54 to 91.29%. SA solution showed a change in saturation of 69.87~94.11 at a concentration of 0.5%, 75.01~94.7 at 1%, 76.05~94.65 at 1.5%, and 85.56~100% at 2%. Among them, 0.5, 1, and 1.5% of SA solutions showed a sharp increase in saturation when the flow rate increased from 10 to 100. On the other hand, water and SA 2% solution showed a relatively constant increase in saturation. In the case of SA 2%, it was confirmed that there was no abrupt increase in the saturation according to the flow rate because it showed a high saturation of 85.56% at a low flow rate. In the case of 1000 μL/min, because it induces a very high injection pressure, 100 μL/min was as the upper bound.

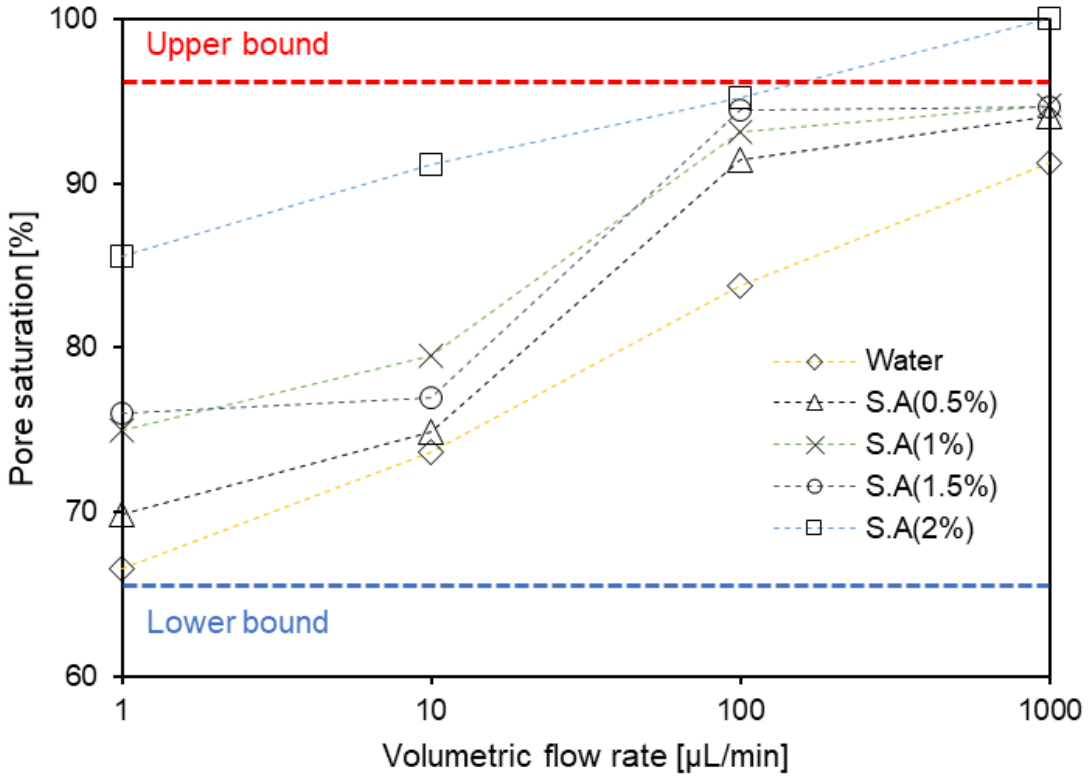

Fig.6 Pore saturation change with SA concentration and volumetric flow rate

Fig.7 shows the power-law parameters n and K index change with the pore saturation of the SA solution when the volumetric flow rate is 1 μL/min. Depending on the SA content, the n and K values were different, and the N, K, and saturation all tended to increase until the SA content was 1.5%. When the SA content became more than 2%, the N value slightly decreased and the K and pore saturation tended to increase. When the SA content is 2% or more, the n value does not increase significantly, and it is judged that the increase in saturation is not large even if the SA content is increased.

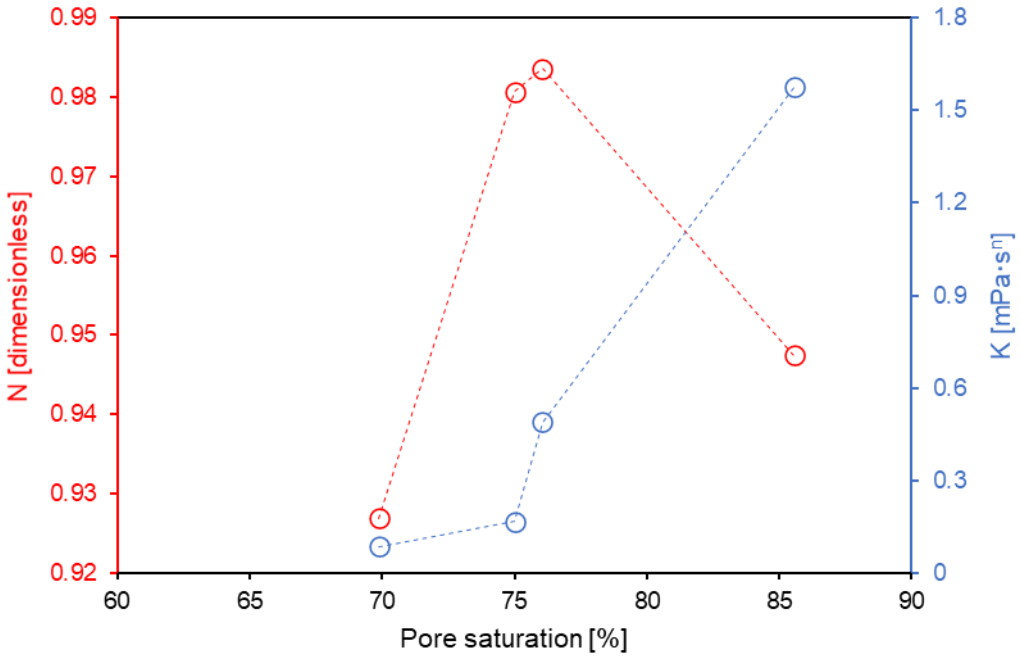

Fig.7 Relationship between power-law parameter and pore saturation

3. CONCLUSIONS

In this study, the model and parameters of the non-Newtonian fluid were determined to analyze the rheological properties affecting the penetration of the SA solution into the ground. In addition, the saturation of the SA solution was analyzed through a micro-scale test. The conclusion is as follows.

- SA solution exhibits shear-thinning behavior with increasing viscosity as the shear rate increases. SA solution showed a tendency to increase both n and K values from 0.5 to 1.5%, but from 2% or more, the n value slightly decreased and the K value increased rapidly. Non-Newtonian fluid has the characteristic of rapidly changing viscosity change with the shear rate. Therefore, it is necessary to clearly determine the in-situ viscosity by determining the effective shear rate considering the field conditions.
  .

- For both SA solution and water, the saturation increased as the injection flow rate increased. At the same injection flow rate, the higher the SA content, the higher the degree of saturation, which can be judged as an increase in viscosity. However, since an increase in viscosity in the actual field may cause fracture due to an increase in injection pressure, it suggests that the content of biopolymer should be adjusted in consideration of field conditions.

ACKNOWLEDGEMENT

This work was supported by the National Research Foundation of Korea(NRF) grant funded by the Korea government. (MSIT) (2020R1A2C1012352).

REFERENCES

Ahn, S., Ryou, J. E., Ahn, K., Lee, C., Lee, J. D., & Jung, J. (2021), "Evaluation of Dynamic Properties of Sodium-Alginate-Reinforced Soil Using A Resonant-Column Test," *Materials (Basel)*, **14**(11). 2743.

Arab, M. G., Mousa, R. A., Gabr, A. R., Azam, A. M., El-Badawy, S. M., & Hassan, A. F. (2019), "Resilient Behavior of Sodium Alginate–Treated Cohesive Soils for Pavement Applications," *J. Mater. Civ. Eng*, **31**(1).

Chang, I., Im, J., Prasidhi, A. K., & Cho, G.-C. (2015), "Effects of Xanthan gum biopolymer on soil strengthening," *Constr Build Mater*, **74**, 65-72.

Chang, I., Prasidhi, A. K., Im, J., & Cho, G.-C. (2015), "Soil strengthening using thermo-gelation biopolymers," *Constr Build Mater*, **77**, 430-438.

Cho, G.-C., & Chang, I. (2018), "Cementless Soil Stabilizer–Biopolymer," Proceedings of the 2018 World Congress on Advances in Civil, Environmental, & Materials Research (ACEM18) Songdo Convensia, Incheon, Korea.

Fatehi, H., Abtahi, S. M., Hashemolhosseini, H., & Hejazi, S. M. (2018), "A novel study on using protein based biopolymers in soil strengthening," *Constr Build Mater*, **167**, 813-821.

Ham, S.-M., Chang, I., Noh, D.-H., Kwon, T.-H., & Muhunthan, B. (2018), "Improvement of Surface Erosion Resistance of Sand by Microbial Biopolymer Formation," *J. Geotech. Geoenviron. Eng.*, **144**(7).

Hwang, S.-p., Yoo, W.-k., & Kim, C.-y. (2018), "Experimental Study on Characteristics of Penetration into Microcrack Depending on Viscosity," *Int J Eng Res Appl*, 227-232.

Jeoung, J.-H., Hwang, S.-P., Lee, J.-H., & Lee, T.-H. (2016), "The study on Evaluation of Injection Performance in Micro Crack Depending on Viscosity of Grouting Material," *J.Korean Soc. Hazard Mitig*, **16**(5), 239-245.

Jung, J., Jang, J., & Ahn, J. (2016)," Characterization of a Polyacrylamide Solution Used for Remediation of Petroleum Contaminated Soils," *Materials (Basel)*, **9**(1).

Jung, J.-W., Cao, S., & Ahn, J. (2014), "Characteristerization of biopolymer solution used for soil remediation and petroleum production," *J.Korean Soc. Hazard Mitig*, **14**(5), 109-114.

Ko, D., & Kang, J. (2020), "Biopolymer-Reinforced Levee for Breach Development Retardation and Enhanced Erosion Control," *Water*, **12**(4), 1070.

Lavrov, A. (2015), “Flow of truncated power-law fluid between parallel walls for hydraulic fracturing applications,” *J Nonnewton Fluid Mech*, **223**, 141-146.

Lee, S., Chang, I., Chung, M.-K., Kim, Y., & Kee, J. (2017), “Geotechnical shear behavior of Xanthan Gum biopolymer treated sand from direct shear testing,” *Geomechanics and Engineering*, **12**(5), 831-847.

Lenci, A., Longo, S., & Di Federico, V. (2020), “Shear-thinning fluid flow in variable-aperture channels,” *Water*, **12**(4), 1152.

Osswald, T., & Rudolph, N. (2015), “Polymer rheology,” Carl Hanser, München.

Wallevik, J. E. (2006) , “Relationship between the Bingham parameters and slump,” *Cem Concr Res*, **36**(7), 1214-1221.